Article:
Moroz, Olga V., Jensen, Pernille F., McDonald, Sean P. et al. (17 more authors) (2018) Structural dynamics and catalytic properties of a multimodular xanthanase. ACS Catalysis. 6021–6034. ISSN: 2155-5435

https://doi.org/10.1021/acscatal.8b00666

Structural Dynamics and Catalytic Properties of a Multi-Modular Xanthanase

Olga V. Moroz[1,=], Pernille F. Jensen[2,=], Sean P. McDonald[3,=], Nicholas McGregor[4], Elena Blagova[1], Gerard Comamala[2], Dorotea R. Segura[5], Lars Anderson[5], Santhosh M. Vasu[5], Vasudeva P. Rao[5], Lars Giger[5], Trine Holst Sørensen[6], Rune Nygaard Monrad[5], Allan Svendsen[5], Jens E. Nielsen[5], Bernard Henrissat[7], Gideon J. Davies[1], Harry Brumer[3,4,], Kasper Rand[2,*] & Keith S. Wilson[1,*]*

1 York Structural Biology Laboratory, Department of Chemistry, the University of York, York YO10 5DD, UK

2 Department of Pharmacy, University of Copenhagen, Universitetsparken 2, 2100 Copenhagen, Denmark

3 Michael Smith Laboratories and Department of Biochemistry and Molecular Biology, University of British Columbia, Vancouver, British Columbia V6T 1Z4, Canada

4 Michael Smith Laboratories and Department of Chemistry, University of British Columbia, Vancouver, British Columbia V6T 1Z4, Canada

5 Novozymes A/S, Krogshojvej 36, DK-2880 Bagsvard, Denmark

6 Department of Science and Environment, INM, Roskilde University, 1 Universitetsvej, DK-4000, Roskilde Denmark

7 Architecture et Fonction des Macromolecules Biologiques, UMR 7857 CNRS, Aix-Marseille University, F-13288 Marseille, France; Institut National de la Recherche Agronomique, USC 1408 Architecture et Fonction des Macromolecules Biologiques, F-13288 Marseille, France; Department of Biological Sciences, King Abdulaziz University, Jeddah, Saudi Arabia

ABSTRACT The precise catalytic strategies used for the breakdown of the complex bacterial polysaccharide xanthan, an increasingly frequent component of processed human foodstuffs, have remained a mystery. Here we present the characterization of an *endo*-xanthanase from *Paenibacillus* sp. 62047. We show that it is a CAZy family 9 glycoside hydrolase (GH9) responsible for the hydrolysis of the xanthan backbone, capable of generating tetrameric xanthan oligosaccharides from polysaccharide lyase family 8 (PL8) xanthan lyase-treated xanthan. 3-D structure determination reveals a complex multi-modular enzyme in which a catalytic $(\alpha/\alpha)_6$ barrel is flanked by an N-terminal "immunoglobulin-like" (Ig-like) domain (frequently found in GH9 enzymes) and by four additional C-terminal all β-sheet domains which have very few homologs in sequence databases and, at least, one of which functions as a new xanthan-binding domain, now termed CBM84. The solution phase conformation and dynamics of the enzyme in the native calcium-bound state and in the absence of calcium were probed experimentally by hydrogen/deuterium exchange mass spectrometry. Measured conformational dynamics were used to guide the protein engineering of enzyme variants with increased stability in the absence of calcium; a property of interest for the potential use of the enzyme in cleaning detergents. The ability of hydrogen/deuterium exchange mass spectrometry to pinpoint dynamic regions of a protein under stress (e.g. removal of calcium ions) makes this technology a strong tool for improving protein catalyst properties by informed engineering.

KEYWORDS Enzyme, carbohydrate. Xanthan, Hydrogen/deuterium exchange mass spectrometry, enzyme stability, enzyme dynamics

INTRODUCTION

Xanthan (Figure 1) is a complex, extracellular hetero-polysaccharide that is produced by bacterial strains from the genus *Xanthomonas*, pathovars of which (e.g. *Xanthomonas campestris* var. *campestris*) are also well-known as causative agents of disease in agriculturally important vegetables[1-2]. Considerable industrial interest in xanthan stems from its favorable rheology modifying properties in applications ranging from food production, petroleum extraction, and pharmaceutical formulation [1, 3]. Indeed, recent estimates indicate that 86 kilotonnes of xanthan are produced by fermentation each year at a value of ca. US$ 400 M[4].

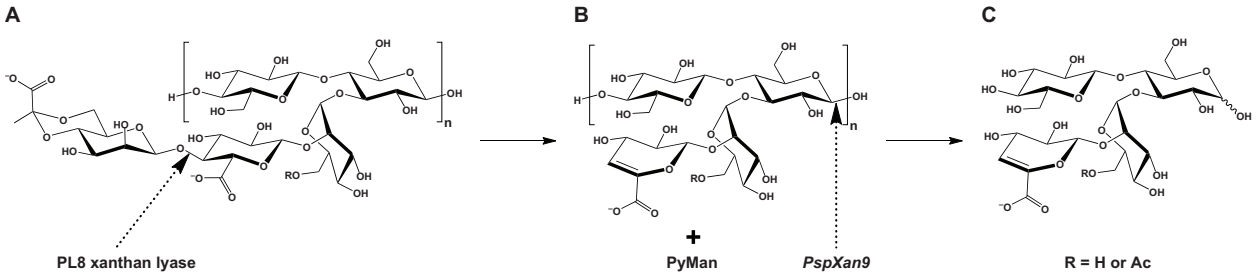

Figure 1 – The structure of xanthan and products following treatment with PL8 xanthan lyase and *Psp*Xan9. Xanthan lyase cleaves the side chain GlcA-β1→4-pyruvylated mannose glycosidic linkage from native "polypentameric" xanthan (A), resulting in the formation of a Δ4,5-*ene*-GlcA residue and release of pyruvylated mannose. The resulting "polytetrameric" xanthan (B) is the preferred substrate for the GH9 *endo*-xanthanase, which yields tetrasaccharides (C) as limit-digest products. Acetylation is variable.

Structurally, xanthan comprises a regular, pentasaccharide-based repeating structure based on a cellulose-like β(1→4)-glucan backbone (Figure 1)[5]. Alternating backbone residues bear a side chain consisting of an inner α(1→3)-mannosyl residue to which a β(1→2)-glucuronic acid residue and terminal β(1→4)-mannosyl residue are attached. This core carbohydrate structure is further

elaborated by the addition of a 6-*O*-acetyl group on the inner α-D-mannosyl residue and a pyruvyl group on the terminal β-D-mannose to create a 4,6-*O*-[(*S*)-1-carboxyethylidene] moiety. Acetylation and pyruvylation occurs on ca. 50% and 30%, respectively, of the pentasaccharide repeating units. The frequency of occurrence depends on the particular *Xanthomonas* strain and on fermentation conditions [6-8].

In light of the notable effects of polysaccharide primary structure on application properties, there is considerable interest in the controlled modification of xanthan during biosynthesis [2] as well as through subsequent enzymatic processing. Our work is therefore focused on the discovery of novel active xanthanases. Furthermore, as the human genome does not encode xanthanases, there is interest in xanthanase discovery in the context of potential polysaccharide fiber degradation by the human microbiota. This aims to aid functional annotation of these organisms. Xanthan-degrading enzymes have been obtained from bacteria, including *Bacillus* sp., *Corynebacterium* sp. (for example ref.[9]), and a mixed culture[10] capable of growth on the polysaccharide. Commensurate with the structural complexity of xanthan, complete saccharification involves sequential action of an extracellular xanthan lyase, an extracellular *endo*-β-glucanase, and three intracellular *exo*-glycosidases: β-glucosidase, glucuronidase, and α-mannosidase[9, 11-14]. Recent whole-genome analysis indicates that some xanthan-utilizing bacteria, exemplified by *Microbacterium* sp. strain XT11, encode these enzymes and requisite sugar transporters via a single, transcriptionally co-regulated gene cluster[15].

The first xanthan-degrading enzymes to be biochemically and structurally characterized in detail were the xanthan lyases (EC 4.2.2.12), which release pyruvylated mannose via eliminative cleavage with concomitant production of a Δ4,5-unsaturated glucuronic acid (Δ4,5-*ene*-GlcA) side chain (Figure 1)[10]. These enzymes were originally purified from a salt-tolerant mixed culture[16],

from a *Bacillus* sp.[17], and *Paenibacillus alginolyticus*[6] and are now defined as members of Polysaccharide Lyase Family 8 (PL8) [18]. The PL8 xanthan lyase from *Bacillus* sp. GL1 presently serves as the lone structural representative of these enzymes, including both substrate and product complexes [19-21].

Xanthan backbone hydrolysis is mediated by specific *endo*-glucanases which generally require the prior action of xanthan lyase to allow attack on the β(1→4)-glucan chain (Figure 1)[9-10, 12] (see [22] for a notable exception). Recent analysis places bacterial *endo*-xanthanases as members of Glycoside Hydrolase Family 9 (GH9)[15], a family more commonly associated with cellulase (unbranched *endo*-β(1→4)-glucanase) activity (EC 3.2.1.4)[23]. Currently, the nature of the structural determinants that confer xanthan specificity among selected GH9 members remains fundamentally unresolved.

To address this issue, we describe here the substrate specificity, crystal structure, and conformational dynamics of *Psp*Xan9, a recently identified GH9 *endo*-xanthanase from *Paenibacillus* sp. 62047.[24] Reflecting previous studies on xanthanases, *Psp*Xan9 is highly specific for lyase-treated xanthan, but is nonetheless weakly active on untreated native xanthan, other (β1→4)-glucans, and (β1→4)-xylans. The crystal structure strikingly revealed that *Psp*Xan9 has a hexamodular tertiary structure that is unique among GH9 members with four calcium-binding sites in the GH9 catalytic domain. The activity and thermostability of *Psp*Xan9 were found to be highly dependent on the presence of calcium ions indicating an important role in stabilizing the protein fold. To assess the solution-phase conformational properties of native *Psp*Xan9 as well as the impact of calcium ion removal, we performed hydrogen/deuterium exchange mass spectrometry (HDX-MS) on the enzyme in the presence and absence of calcium ions. Differential deuterium uptake between the two states revealed increased dynamics /

solvation of backbone amide hydrogens in the absence of calcium near the calcium ion environment detected in the crystal structure. Additionally, the absence of calcium resulted in large increases in dynamics of the β3 domain and in regions of the C-terminal domain that are disordered in the crystal structure. Remarkably, we found that calcium ion removal in three regions leads to the occurrence of distinct populations of *Psp*Xan9 with slow refolding kinetics in comparison to the native state, strongly indicating the presence of additional calcium binding sites in the C-terminal CBM84 domain. Finally, we used the dynamic information obtained by HDX-MS to guide rational engineering of *Psp*Xan9 variants with increased detergent stability.

RESULTS AND DISCUSSION

Enzyme cloning, expression and domain composition

Several xanthan degrading bacterial strains were isolated from forest soil samples grown using xanthan gum as sole carbon source, similarly to Ref.[9]. The gene encoding the *Psp*Xan9 was subsequently amplified by PCR from genomic DNA of the bacterium *Paenibacillus* sp. 62047, isolated from a forest soil sample collected in China and shown to have xanthanase activity.[24] Sequencing of 16S rRNA from this *Paenibacillus species*, revealed 99% identity to *Paenibacillus nanensis* (ARBSILVA:AB265206).

The *Psp*Xan*9* gene was cloned*,* expressed in *Bacillus subtilis* and purified as described in Materials and Methods. The gene sequence coding for *Psp*Xan9 was deposited in GenBank with accession No. MG661269. Sequence analysis, based on PSI-BLAST searches and examination of the CAZy database indicated the enzyme was made up of the following six domains (domain boundaries are approximate): 1-90: Ig-like (we term X229) domain present at the N-terminus of most GH9 enzymes, 91-559: $(\alpha/\alpha)_6$ catalytic module (GH9 in CAZy), 560-914: set of three β domains (β1;

560-657, β2; 658-814 and β3; 815-918) also found in a GH9 protein with accession code BAJ75824.1 [MTES_2860 *Microbacterium testaceum* StLB037; 43% sequence identity]. The *Psp*Xan9 sequence terminates with a domain, 915-1055, which shows low sequence similarity to a variety of CBMs, including CBM6.

We were intrigued whether this C-terminal domain, which is also found on other Xanthan-active enzymes, might function as a novel xanthan-binding module. Xanthan-gum binding assays, Supporting Figure S1, indeed show a xanthan binding function and so this domain forms the root for a new CBM family termed CBM84. Preliminary experiments, in which this domain is removed, do not appear to reduce the activity of the *Psp*Xan9 enzyme on xanthan in the presence of xanthan lyase (data not shown).

Notably, the PspXan9 catalytic domain sequence forms, with several others, a distinct sub-group within GH9, characterized by much higher scores, better e-values, and a percentage of identity higher than approximately 50% with the query suggesting that it defines a sequence that can now be used for function prediction of related sequences. Close examples include previously "hypothetical proteins from *Paenibacillus* and *Cohnella* sp. (accession codes WP_079417835.1, WP_094047237.1, PRX68885.1, WP_082927563.1 all with over 62% sequence identity).

Catalytic activity and specificity of recombinant PspXan9

*Psp*Xan9 hydrolysis activity exhibited a strong dependence on the presence of Ca^{2+} ions in reactions at 37°C in pH 7 HEPES-NaOH buffer (based on preliminary research on *Psp*Xan9 [24]). The maximum activity was obtained with 2 mM $CaCl_2$, after which a monotonic decrease was observed (Figure S2a). In temperature optimization assays containing pH 7 HEPES-NaOH buffer

and 2 mM $CaCl_2$, *Psp*Xan9 had the highest activity at 63°C, but was also rapidly inactivated at temperatures immediately above this (Figure S2b). Therefore, the pH-rate profile was conducted at 55°C to avoid any heat inactivation and resulted in data points forming an approximately bell-shaped appearance, with the highest activity achieved at pH 7.0-7.5 in HEPES-NaOH buffer (Figure S2c).

Further analysis revealed that thermostability during long-term incubations of the enzyme was, like activity, greatly improved in the presence of Ca^{2+}. Specifically, incubation of diluted *Psp*Xan9 in the absence of Ca^{2+} ions at temperatures between 45-69°C led to a rapid decline in activity in all samples, with a 40% loss of activity at 45°C after 1 h (Figure S2a,b). In contrast, incubation of the enzyme with 20 mM $CaCl_2$ gave no detectable loss in activity over 1 h at temperatures up to 60°C, while at 54°C *Psp*Xan9 retained > 75% activity after 48 h (Figure S3c,d). In consideration of these data, 55°C was selected for subsequent kinetic analyses.

*Psp*Xan9 demonstrated a clear preference for lyase treated xanthan compared to all other polysaccharides tested, including native, polypentameric xanthan, as displayed by a 630-fold greater specific activity (Table 1, *cf.* Figure 1). Paenibacillus sp are known to express xanthan lyaes, (including the strain used here[25]. Hydrolysis of the artificial (β1→4)-glucan derivatives carboxymethyl cellulose and hydroxyethyl cellulose, as well as cereal mixed linkage (β1→3)/(β1→4)-glucan, had similarly poor specific activities to native xanthan. Likewise, the highly branched (β1→4)-glucan, xyloglucan [26], and (β1→4)-xylans [27] were feebly hydrolyzed by *Psp*Xan9 (Table 1). Initial-rate kinetics of the hydrolysis of the dominant substrate, lyase-treated xanthan, were readily fit by the classic Michaelis-Menten equation (k_{cat} = 1.69 x 10^4 min^{-1}, K_m = 0.0962 $mg{\cdot}mL^{-1}$; Figure S4).

Table 1. Kinetic analysis of the activity of *Psp*Xan9 on polysaccharide substrates.

Polysaccharide	Specific Activity (U mg^{-1})*
polypentameric xanthan (Figure 1)	0.285 ± 0.010
lyase-treated xanthan (Figure 1)	181 ± 9
CMC	0.492 ± 0.022
HEC	0.180 ± 0.099
bMLG	0.213 ± 0.029
tXyG	0.0679 ± 0.0005
bGX	0.0614 ± 0.0014
wAX	0.0449 ± 0.0132

*One enzyme unit (U) is defined as the amount of enzyme required to release 1 μmol of glucose reducing-end equivalents per minute.

Structural Analysis of PspXan9 Products

HPSEC-UV analysis of the degradation of lyase-treated xanthan by *Psp*Xan9 over time indicated that the enzyme acts processively, rapidly releasing short oligosaccharide products without releasing the polysaccharide chain (Figure 2a & S5). The polysaccharide (elution time 19.1 min, Figure S5a) was initially converted to produce a pair of partially resolved peaks eluting at 32.4 and 33.2 min, the former of which was converted to the latter upon extended (9.5 h) incubation (Figure S5b-f). To identify the products giving rise to these two peaks, samples collected after 2 h and 9.5 h of incubation (Figure 2a & S5e) were analyzed using LC-ESI-MS.

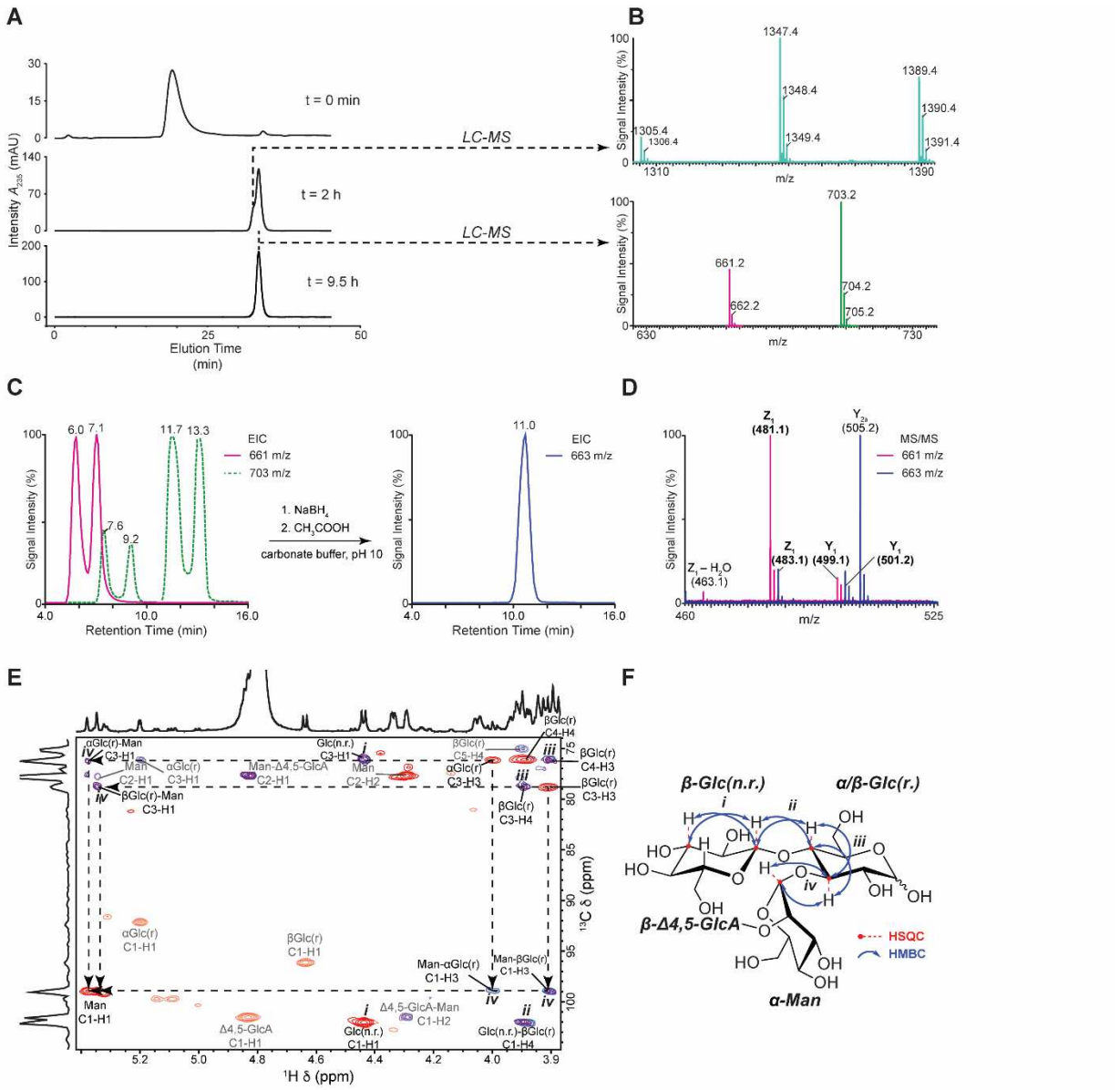

Figure 2 – Complete product analysis of xanthan oligosaccharides produced from the digestion of lyase-treated xanthan by *Psp*Xan9. *A*. HPSEC-UV analysis of products from a time course digestion. Limit digest products are observed following 9.5 h of incubation (see Figure S5 for a full time-course). *B*. Mass spectrum of the unsaturated octasaccharide product (turquoise) found at 32.4 min elution time after a 2 h incubation, and the mass spectrum of acetylated (green) and unacetylated (magenta) unsaturated tetrasaccharides found in the partial digest (2 h) and the limit digest (9.5 h) and eluting at 33.2 min (see Figure S6 for chromatograms). *C.* Extracted ion chromatograms showing the acetylated (green) and unacetylated (magenta) unsaturated tetrasaccharides limit digest products and their subsequent reduced and deacetylated form (blue) after treatment with $NaBH_4$. Two chromatographic peaks were observed for each species due to

the resolution of reducing-end anomers. *D*. MS/MS results comparing the unacetylated unsaturated tetrasaccharide (magenta) and the $NaBH_4$-reduced derivative (blue), with key ion fragments identified above their corresponding masses (see Figure S6-S8 for full MS/MS spectra). *E*. The diagnostic region of the $^{1}H,^{13}C$ HSQC and HMBC 2D-spectra for the identification of the *Psp*Xan9 products (see Figure S12 for full 2D-heteronuclear NMR spectrum). Each red crosspeak corresponds to a $^{1}J_{C,H}$-coupling interaction from the HSQC experiment. $^{2}J_{C,H}$- or $^{3}J_{C,H}$-couplings were generated with HMBC experiments optimized for couplings at 5 Hz or 10 Hz, and are represented by blue and purple crosspeaks, respectively. The dotted arrows aid in tracing the path between the red HSQC crosspeaks of both of the C3-H3 peaks from the α/β-glucose reducing end (Glc(r.)) glucose through blue/purple HMBC crosspeaks to the red HSQC crosspeak of the C1-H1 of mannose. *F*. Structure of the unsaturated xanthan tetrasaccharide and key 2D-heteronuclear interactions illustrating those as seen in panel *E*. Note, for panels *E-F*, roman numerals *i-iv* show important correlations and their position within the unsaturated xanthan tetrasaccharide. Abbreviations used: r., reducing end; n.r., nonreducing end; Glc, glucose; Man, mannose; Δ4,5-GlcA; Δ4,5-*ene*-GlcA. Note, for panels *B-D* colors correspond to isolated products with turquoise being unsaturated xanthan octasaccharides, magenta being unacetylated unsaturated tetrasaccharides, green being acetylated unsaturated tetrasaccharides and blue being reduced de-/un-acetylated unsaturated tetrasaccharides. The notation states the sugar residue and its corresponding atom(s) below it. The sugar residue containing the carbon atom is always listed first, followed by the residue containing the proton atom. However, if both carbon and proton atoms exist within the same residue, the residue is only listed once.

LC-ESI-MS analysis of the 9.5 h sample revealed that the primary limit-digest products were the unsaturated tetrasaccharide (661 m/z) and two mono-acetylated derivatives (703 m/z; Figure 2b & 2c, *cf*. Figure 1c). Detailed analysis of the 2 h sample likewise indicated the presence of these two products (Figure 2b & S6b-c), in addition to masses consistent with non- (1305m/z), mono- (1347 m/z), and di-acetylated (1389 m/z) octasaccharides corresponding to dimers of the tetrasaccharides (Figure 2b & S6f-h). The presence of both tetra- and octasaccharide products indicates that *Psp*Xan9 is capable of cleaving lyase-treated polytetrameric xanthan (Figure 1) at intervals of either two or four backbone glucose residues, and rationalizes the observation of two low-M_w peaks in the HPSEC (Figure 2a & S5). In addition to these major products (Figure S6b-c & f-h), extracted-ion chromatograms revealed the presence of low levels of monoacetylated, depyruvylated pentasaccharide (883 m/z) (Figure S6d), and di-acetylated, depyruvylated pentasaccharide (925 m/z) (Figure S6e) resulting from incomplete cleavage of the native

polysaccharide by the xanthan lyase (Figure 1), which showed high specificity for pyruvylated mannose [17].

Reduction of the limit-digest products with $NaBH_4$ resulted in the conversion of the non- and monoacetylated tetrasaccharides to a single alditol product of 663 *m/z* (Figure 2c). The location of the side chain was indicated by individual MS/MS analysis of the 661 and 663 *m/z* precursor ions of the tetrasaccharide and alditol, respectively (Figure 2d & S7-S8). Diagnostic product ions from the reducing-end glucose and glucitol were identified by the corresponding Δ *m/z* of 2. These included Y_1 (481 vs. 483 *m/z*) and Z_1 (499 vs. 501 *m/z*) ions (Figure 2d, see Figure S7-S8 for fragment structures). The presence of a B_1 ion of 161 *m/*z and a C_1 ion of 179 *m/z* in both MS/MS spectra (and absence of a Y_1 ion of 181 *m/z* and Z_1 ion of 163 *m/z* in the alditol) further suggested that the side chain emanated from the reducing-end Glc, as indicated in Figure S7-S8.

To provide further support for the proposed structure of the unsaturated tetrasaccharide, a series of NMR analyses were conducted. A combination of selective ^{1}H 1D-TOCSY, ^{1}H 2D-TOCSY and COSY experiments (Figure S9-S11) allowed for a complete proton assignment, including coupling constants and multiplicities (Table S1). Identification of the spin systems corresponding to individual monosaccharide residues was accomplished by individually irradiating anomeric protons between δ 4.29-5.36 ppm (Figure S9a) using selective ^{1}H 1D-TOCSY experiments (Figure S9b-g)[28-29]; the identities of the anomeric protons were inferred from literature values [29] or authentic standards (data not shown). Of particular note, the α-mannosyl residue presented two anomeric protons as apparent singlets at δ 5.35 and 5.38 ppm ($^3J_{H1,H2}$ < 1 Hz, Table S1). Simultaneous irradiation of these peaks was insufficient to reveal the complete α-mannose spin system, due to weak equatorial coupling via H2 (Figure S9e). In contrast, irradiation of H2 (δ 4.29 ppm) revealed all of the Man ring protons (Figure S9f) as well as the two singlets. The appearance

of two anomeric signals, and the complexity of the H3-H5 peaks (Figure S9f) is suggestive of conformational flexibility of this core mannosyl unit.

Irradiation of a peak within the anomeric range at δ 4.34 ppm revealed the Δ4,5-*ene*-GlcA ("Δ4,5-GlcA" in Figures 2, S9, S12-S13) spin-system and was later determined to be H3 through ^{1}H 2D-TOCSY and COSY experiments (Figure S9g & S10-S11). These techniques also allowed the assignment of the Δ4,5-*ene*-GlcA anomeric peak which was buried beneath the HOD peak (δ 4.73 ppm; Figure S10-S11). Interestingly, the anomeric proton of the β(1→2)-linked Δ4,5-*ene*-GlcA, also appeared as two doublets, further suggesting distinct conformers.

Most ^{13}C assignments were inferred by matching proton chemical shifts with $^{1}J_{C,H}$ correlations in HSQC experiments (Figure S12; Table S1). However, to determine the carbohydrate sequence and the full ^{13}C assignment of Δ4,5-*ene*-GlcA (due to the lack of $^{1}J_{C,H}$ present of Δ4,5-*ene*-GlcA C5 and C6), HMBC experiments were performed to obtain $^{2}J_{C,H}$- and $^{3}J_{C,H}$-couplings. This allowed information about glycosidic linkages ($^{3}J_{C,H}$-coupling) and the assignment of Δ4,5-*ene*-GlcA C5 and C6 through the presence of $^{2}J_{C5,H4}$ and $^{3}J_{C5,H3}$ crosspeaks for C5 and $^{3}J_{C6,H4}$ crosspeaks for C6 (Figure S13).

Information regarding glycosidic bonds was provided by pivotal correlations including the linkages between C1 of the non-reducing-end Glc, Glc(n.r), and H4 of the β-anomer of the reducing-end Glc,β-Glc(r.), *i.e.* ($^{3}J_{\text{Glc(n.r.)-C1,β-Glc(r.)-H4}}$), as well as between C3 or H3 of α/β-Glc(r.) and the mannosyl anomeric centre ($^{3}J_{\text{Man-C1,α/β-Glc(r.)-H3}}$; $^{3}J_{\text{α/β-Glc(r.)-C3,Man-H1}}$) (Figure 2e-f & S12). Lastly, position 3 of the Glc(n.r) only has intra-residue HMBC correlations, and thus lacks any correlations with chemical shifts matching the mannosyl anomeric centre. This provides strong evidence of the absence of a side chain at this position.

Together, the MS and NMR data suggest that *Psp*Xan9 specifically hydrolyzes the β(1→4)-glucan backbone of tetrapolymeric xanthan at the glucosidic bond of the branched glucosyl residues, *i.e.* those appended with β(1→2)-Δ4,5-*ene*-glucuronyl-α(1→3)-mannosyl side chains (Figure 1). This specificity was previously observed for an endo-xanthanase from *Bacillus* sp. GL1 by sequential enzyme degradation[9]. This specificity is distinct from xanthan-active cellulases (endo-β(1→4)glucanases), which have been shown to hydrolyze the native polysaccharide at non-branched Glc residues to produce pentasaccharides[30-31].

3-D structure of an endo-xanthanase

The structure of *Psp*Xan9 was solved using single isomorphous replacement with anomalous scattering from a $K_2Pt(SCN)_4$ derivative and was refined at 2 Å resolution (Table S2). The structure displays a complex six-domain organization as introduced above (Figure 3). The C-terminal CBM84 domain is comprised of highly disordered residues (919-1055) and therefore could not be traced unambiguously in final structure. For this reason, the residues in the three unconnected β-strands of the CBM84 domain are described as unknown (UNK) in the final model.

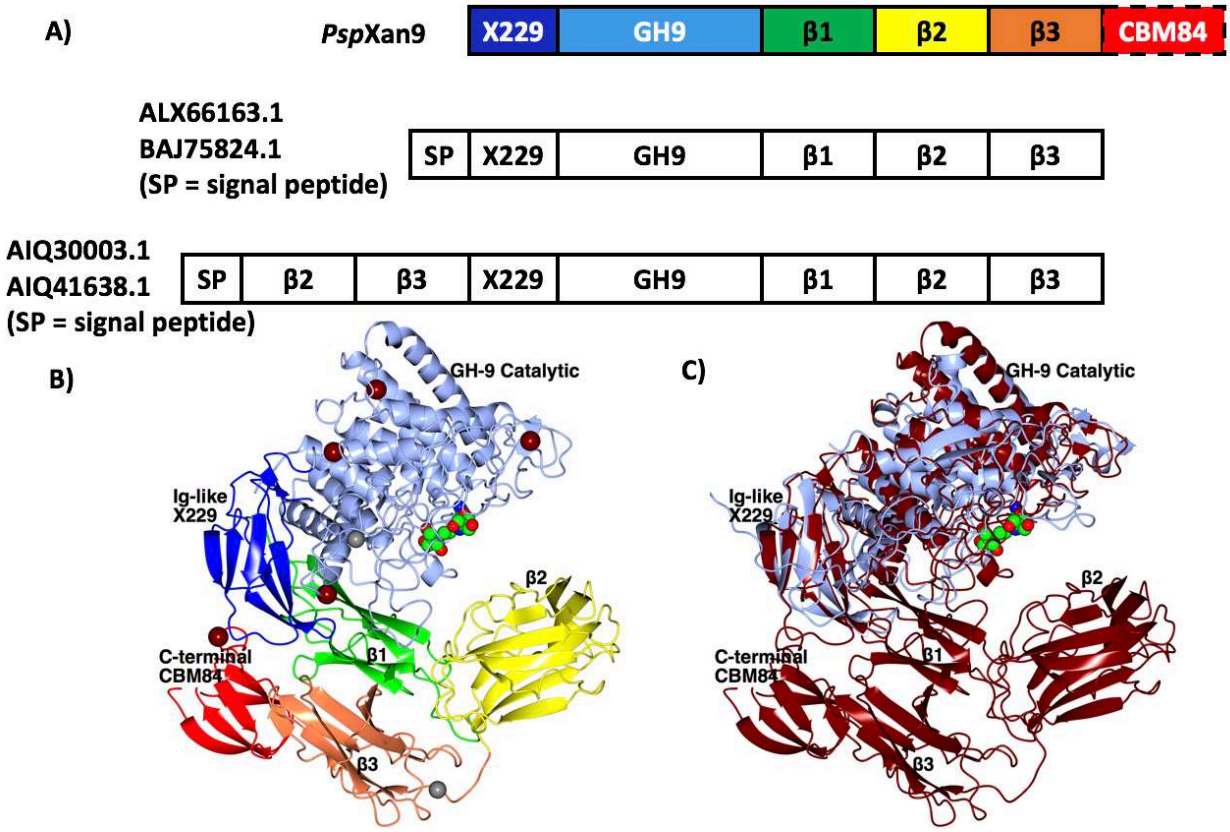

Figure 3 – Overall organization of *Psp*Xan9. **(A)** Schematic showing the organization of the domains from *Psp*Xan9 (domains colored as in (B). **(B)** Ribbon representation of the overall fold colored by domain, from the N-terminus: Ig-like, X229 domain (1-90) (blue), GH9 catalytic module (91-559) (ice blue), β1 (560-657) (green), β2 (658-814) (yellow), β3 (815-914) (coral), CBM84 domain (915-1055) (red). The calcium ions are shown as brown spheres, sodium as grey. Bis-Tris-Propane (BTP) indicates the location of the ligand binding site, shown as spheres colored by atom. **(C)** Superimposition of *Psp*Xan9 (brown) with 1CLC, the endonuclease D from *Ruminiclostridium thermocellum*.

The first two domains are typical of GH9 enzymes. The most similar structure to the catalytic domain is the *endo*-glucanase CelD from *Ruminiclostridium thermocellum* (PDB code 1CLC) with an r.m.s.d of 2.0 Å for 464 equivalent Cα atoms (superposed using SSM[32] within CCP4mg[33], (Figure 3c) with which *Psp*Xan9 shares around 20% sequence identity. The three all-β domains (Figure 3a) are absent from 1CLC. Sequence homology is shared between *Psp*Xan9 and the GH9 protein with accession code BAJ75824.1 [MTES_2860 *Microbacterium testaceum* StLB037; 43%

sequence identity] which has an equivalent region containing all three β domains (residues 561-918 of MTES_2860), but lacks the C-terminal CBM84 domain (915-1055). Interestingly, apart from this there is a single example of two of the β domains found together, at the N-terminus of sequence entry ALQ30003.1 (Figure 3a).

Several electron density peaks have been modelled as metal ions (Figure 3b), with five metals annotated as calcium based on geometry and B-factors, and more importantly by small but significant peaks in the anomalous difference Fourier. The GH9 family of endoglucanases are extracellular enzymes secreted by both bacteria and eukaryota with structures of 16 family members currently reported in the CAZY database. Many of these contain one or more calcium ions assumed to enhance their stability, while the number of calcium sites varies considerably between enzymes. For example, the endoglucanase from *R. thermocellum* (PDB 1CLC) contains three calciums plus a zinc ion, while endoglucanase 9g from *Clostridium cellulolyticum* (PDB 1G87) has two calciums, together with three magnesium ions. The positions of the calcium sites are not widely conserved across the family. The first Ca^{2+} ion does correspond to a Ca^{2+} ion found in 1CLC, and is coordinated by the main chain of Ile197 and the side chain oxygens from Asp191, Asp193, Asn195, Asp199, and Asp202 that form a calcium binding loop in the GH9 domain. The other three metal (two calcium and one zinc) sites from 1CLC are absent in *Psp*Xan9. There is a possible Ca^{2+} bound to Glu923 and Glu925 from the CBM84 domain, plus some unidentified residues within this domain, but the quality of the electron density in that region is not good enough to model these residues with confidence. This is highly significant in light of the HDX-MS analysis in the presence and absence of Ca^{2+} described below.

The active site is an open cleft typical for *endo*-acting glucanases[34]. Comparison with a representative GH9 family protein-ligand complex structure (1GA2, *endo*-glucanase Cel9G from

Ruminiclostridium cellulolyticum complexed with cellobiose[35], shows the expected close similarities in location and conformations of the catalytic residues, as well as a number of other ligand binding residues (Figure 4a). The conserved catalytic residues are Glu536, acting as an acid, and Asp158 or Asp161 as putative bases in an inverting mechanism. Some residues differ between Psp and cellulose-active GH9s, *e.g.* Glu424 instead of Arg315, which coordinates the ligand in 1GA2, and Phe420 which replaces Trp311 in the –2 subsite (Figure 4a). Unlike 1GA2 and 1KFG (a thio-oligosaccharide complex of *R. cellulolyticum,* Cel9G), the binding cleft of *Psp*Xan9 is shallower and partly shielded on the outside by the second and third subdomains of the all-β domain 3 (Figure 4b.

A)

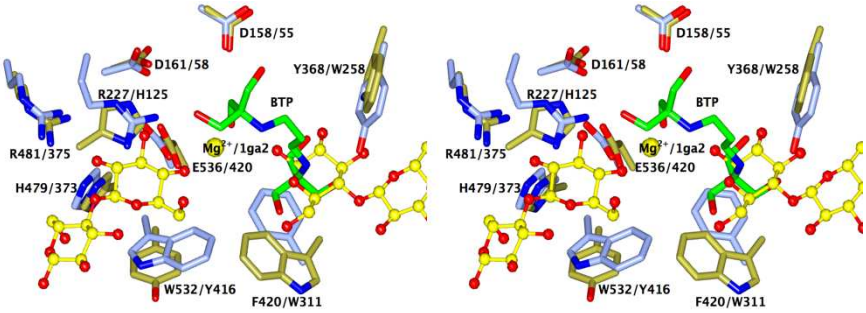

B)

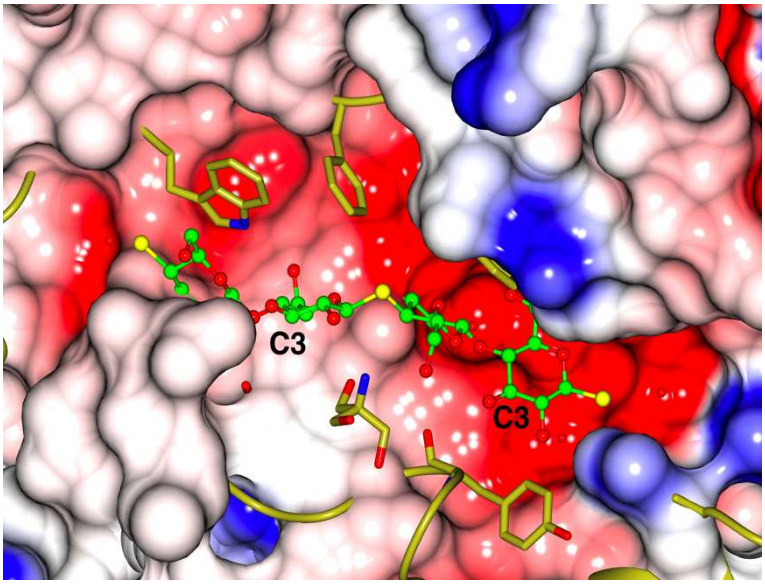

Figure 4 – The active site. (A) Stereo view of the binding site of *Psp*Xan9 superposed on the corresponding region of *endo*-glucanase Cel9G from *Ruminiclostridium cellulolyticum* (1GA2). Residues are shown as cylinders, ligands as ball and stick, and metal ions as spheres. The amino acids are colored by atom but with the carbon atoms in ice blue (*Psp*Xan9) and gold (1GA2). The left-hand number refers to the residue in *Psp*Xan9 followed by that for 1GA2. The cellobiose ligands are shown in yellow in ball and stick, and the magnesium and BTP are from *Psp*Xan9. **(B)** The active site of *Psp*Xan9 shown as an electrostatic surface. This was superposed on the equivalent region of the tetrasaccharide complex of the Cel9G from *R. cellulolyticum* (1KFG), with the saccharide shown in ball and stick colored by atom, and the surrounding residues in gold. The ligand occupies the –4 to –1 sugar-binding subsites, and the C3 atoms of residues –1 and –3 are labelled.

Attempts were made to co-crystallize the enzyme with xanthan tetrasaccharide, but these experiments were unfortunately, unsuccessful, so to investigate whether there is space to accommodate the larger xanthan ligand in the active site of *Psp*Xan9, we superimposed its structure with that of the tetrasaccharide complex of the Cel9G from *R. cellulolyticum* (1KFG), (Figure 4b). The site is much more open in *Psp*Xan9, and there is considerable space around the ligand which should easily be able to accommodate the xanthan side chains.

Conformational Dynamics of *Psp*Xan9 Measured by Solution-Phase HDX-MS.

The conformation and dynamics of *Psp*Xan9 in solution were determined by monitoring the hydrogen/deuterium exchange of backbone amide groups of a protein by mass spectrometry. In *Psp*Xan9 the local (peptide level) HDX-MS analysis reports on the conformational dynamics of 99% of the backbone amide hydrogens that are covered by 267 overlapping peptic peptides (Figure S14 & S15). Considering the HDX of *Psp*Xan9 over the 1 h time course, it was evident that there are major differences in regional deuterium uptake and thus dynamics in the protein (Figure 5). In the Ig-like (X229) domain, fast HDX is observed in residues 46-5 (>80% D) and 67-76 (>90% D), whereas for the domain GH9, residues 187-190 (100% D), 274-291 (>80% D), 309-332, (>80%

D) and 416-420 (100% D) show fast HDX. Region 187-190 is in close proximity to the calcium ion, coordinated by Asp191, Asp193, Asp195, Asp199 and Asp202.

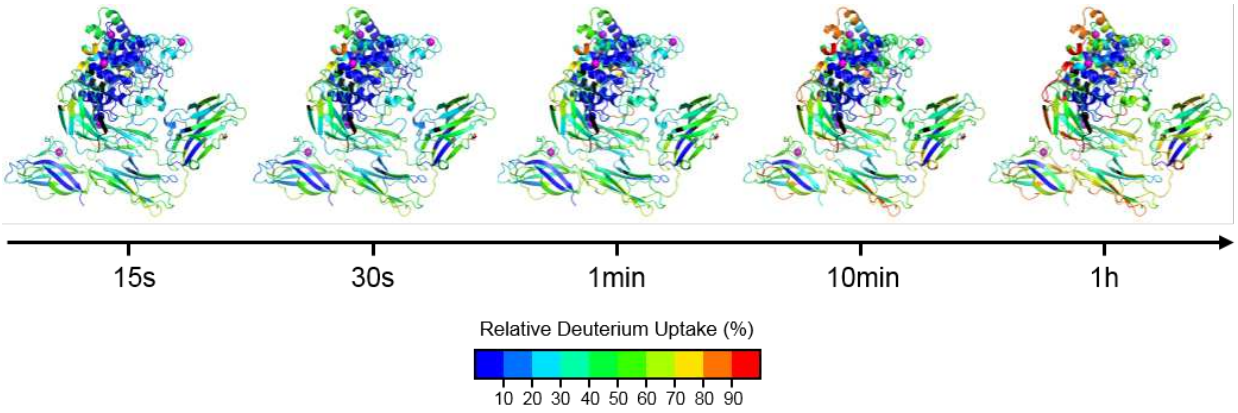

Figure 5 - Solution-phase conformational dynamics of *Psp*Xan9. The relative deuterium content of *Psp*Xan9 at the labeling time intervals 15 s, 30 s, 1 min, 10 min and 1 h was adjusted to the fully deuterated control and mapped on the X-ray crystal structure according to the indicated color scale. Regions without HDX information are shown in grey. The calcium and platinum ions are shown in magenta and green spheres, respectively.

At shorter time points, for example 15 s, the loop connecting GH9 domain and β1 (res. 554-566) show more than 50% deuterium uptake increasing to more than 90% after 1 h. Notably, the position of S560 is not visible in the crystal structure reflecting this intrinsic flexibility. The loop (res. 588-600) in the β1 domain also show a similar pattern in going from more than 50% to 90% over the HDX time course with deuterium uptake extending to residues 588-611.

Domain β3 and parts of the nearby β2 show some of the most pronounced dynamics. At the earliest sampling time point of 15 s, residues 811-822 and 869-883 of β3 show more than 50% deuterium uptake. After 1 h HDX this deuterium uptake increases to over 80% and has propagated to nearby regions 845-856 and 898-906 in β3 and region 775-782 in β2. The loop 764-782 show more than 80% deuterium incorporation after only 15 s indicating highly dynamics nature and solvation. In

the CBM84 domain (Table S3), which is significantly disordered in our crystal structure, the largest deuterium uptake after 1 h was observed for residues 965-972 (90%), 991-1012 (>80%), 1013 (>70%), 964 (>70%). These, as well as residues 1015-1026 all show deuterium uptake over 50% after 15 s HDX, indicating significant solvation and a highly dynamic nature; consistent with the crystal structure observation.

Impact on Conformational Dynamics of Calcium Ion Removal by EDTA Chelation.

As described above, the stability of *Psp*Xan9 is dependent on the presence of calcium ions. To understand further the role of calcium on the conformation and dynamics of *Psp*Xan9, we measured the HDX of *Psp*Xan9 in the presence of the divalent cation chelator EDTA (Figure 6, Figure 7 and Table S4).

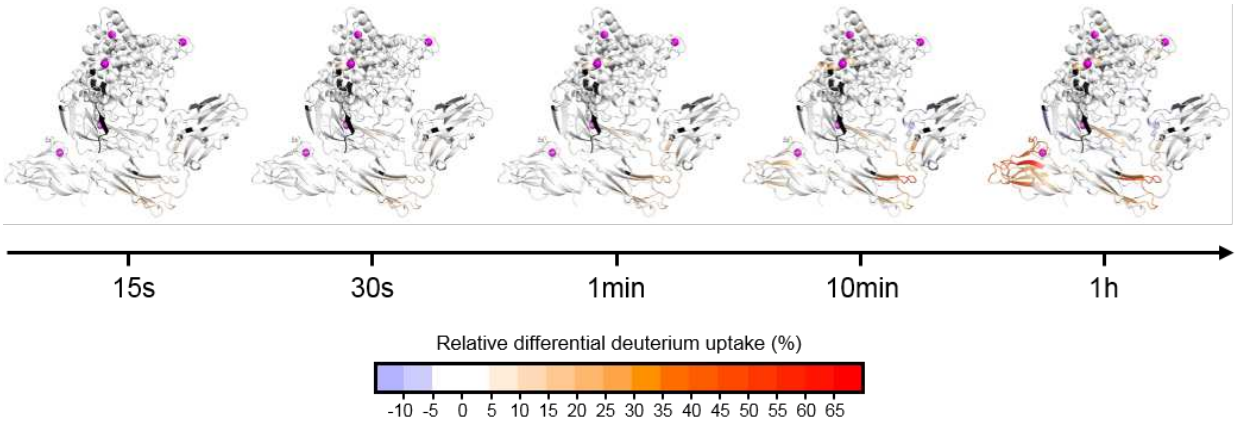

Figure 6 - Solution-phase conformational dynamics of *Psp*Xan9 in the presence of 10 mM EDTA. The relative deuterium content of *Psp*Xan9 in the presence of 10 mM EDTA at the labeling time intervals 15 s, 30 s, 1 min, 10 min and 1 h was adjusted to the fully deuterated control and mapped on the X-ray crystal structure according to the indicated color scale.

Backbone amide hydrogens in the vicinity of all sites shown in the X-ray structure of *Psp*Xan9 to coordinate calcium ions were impacted by EDTA treatment. The two calcium binding loops in the GH9 domain show minor, but statistically significant, increases in deuterium uptake at the 1 h time

point with region 192-200 and 228-251 showing a 2.5% and 5% increase, respectively. In the structured calcium binding site in the interface between GH9 and the β1 domain the region 640-647 containing Tyr641 and Ser642 show an increase in deuterium uptake from 2.5% to 15% during 1 h HDX. Thus, Ca^{2+} has a local stabilizing effect on the conformation of *Psp*Xan9 in these regions. In contrast, the region 406-414 covering the calcium binding residues Asp407 and Glu408 shows decrease in deuterium uptake of 2.5% after 10 min and 1 h labelling. Interestingly, residues 567-570 in the nearby loop show the largest decrease in deuterium uptake of 7.5% when *Psp*Xan9 is treated with EDTA. Local decreases in HDX in the presence of EDTA indicates that Ca^{2+}-coordination in these regions constrains several backbone hydrogens in an exposed exchange-competent conformation, which in turn collapses into a more protected conformation in the absence of the divalent cation.

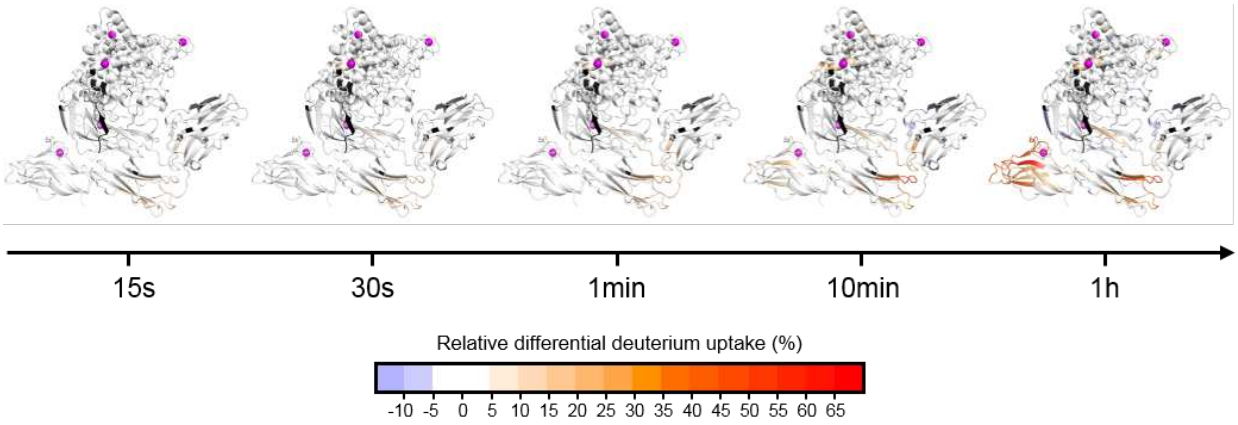

Figure 7 - Impact of calcium ion removal on the conformational dynamics of *Psp*Xan9. Differential deuterium uptake in *Psp*Xan9 in the native state and in the presence of 10 mM EDTA. Residues with a positive relative differential deuterium uptake have increased HDX in the presence of EDTA in comparison to native *Psp*Xan9 and vice versa for a negative relative differential deuterium uptake. Regions without HDX information are shown in dark grey.

Surprisingly, domain β3 showed the largest, earliest and most widespread effects upon calcium ion removal. Region 869-833 shows the highest differential increase in deuterium uptake in the

Ca^{2+} depleted state after 15 s of HDX, with an increase of 10%, which in turn decreases to 5% after 1 h. Residues 841-844, 845-856 and 897-906 all showed a differential increase in deuterium uptake starting at 5% at the first time point and ending above 20%, 25% and 55%, respectively at the final 1 h time point. No calcium ions could be assigned in this area of the crystal structure. However, inspection of the sequence of the perturbed regions, reveals the presence of Asp901 and Asp846 (which is located in a loop in close proximity, 845-856) which bind a metal-ion currently modelled as Na^{+} (on the basis of weak density) which we predict is likely to be a Ca^{2+} binding region.

In the CBM84 domain, there are several regions where backbone amide hydrogens undergo correlated exchange kinetics (EX1 kinetics) in the presence of EDTA indicated by characteristic bimodal isotopic distributions (Figure 8). The occurrence of both a protected and a fully exchanged population reveals that some backbone amide hydrogens in these regions have rates of closing (k_{cl}) much lower than the chemical exchange rate (k_{ch}). Thus, the slow refolding rate of these regions leads to complete deuteration of the backbone amide hydrogens upon one unfolding event and thus reports directly on the rate of opening (k_{op}) of the affected residues. This is in contrast to the exchange kinetics observed in all other regions in *Psp*Xan9 where the k_{cl} is much higher than k_{ch} and thus several opening events take place before the backbone amide hydrogens are completely deuterated (EX2 kinetics). The correlated unfolding dynamics of the three regions all occur with relatively slow rates (k_{op}) with half-lives of the slow-exchanging protected population between 10 min and 1 h. Furthermore, about 14-15 backbone amide hydrogens in peptide 928-959, 9 in 973-989 and 11-12 in 1028-1048 can be seen to be involved in the correlated and slow unfolding/refolding dynamics. The slow correlated unfolding kinetics seen for residues of region 973-989 can be narrowed down to residues 980-989 as the overlapping peptide 973-979 only show

unimodal exchange kinetics (EX2), correlating well with the measured number of amides showing EX1 kinetics.

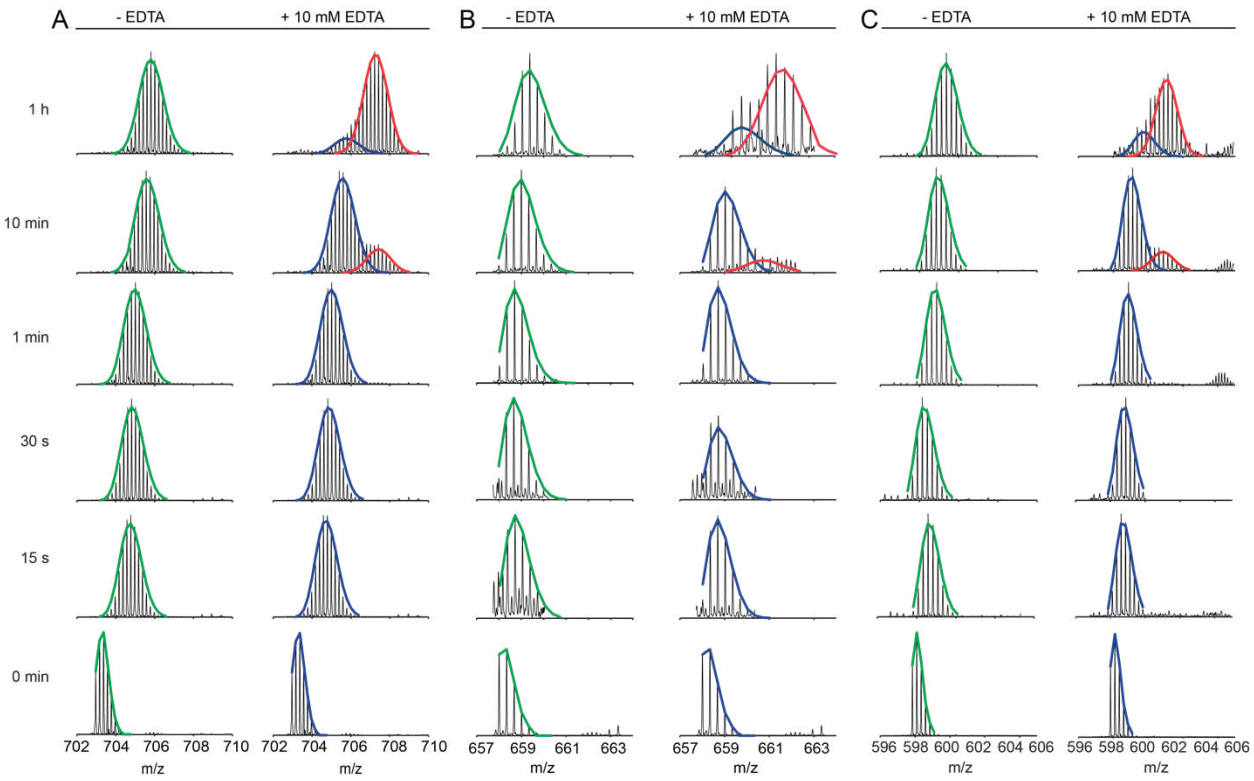

Figure 8 - Slow and correlated unfolding dynamics of the C-terminal CBM84 domain of*Psp*Xan9 in the absence of Ca^{2+}. MS spectra of *Psp*Xan9 in the presence and absence of 10 mM EDTA at the time interval from 0 min to 1 h for peptide A) 928-959 (MH^{5+}), B) 973-989 (MH^{3+})and C) 1028-1048 (MH^{3+}). The raw data were fitted to a binominal isotopic distribution (population1: blue curves, population 2: red curves).

The pronounced impact of Ca^{2+} removal on this domain strongly suggests that there is indeed at least one calcium binding site in the CBM84 domain. The X-ray structure, supported by a weak but significant anomalous scattering signal, indicated the presence of at least one Ca^{2+} site in the CBM84 domain, coordinated by side chain oxygens of what we believe are Glu923 and Glu925 and Asp1047.

Generation of Stable *Psp*Xan9 Variants in the Absence of Calcium Ions

The xanthan degrading properties of this class of enzyme leads to potential applications in cleaning detergents. However, to increase washing performance, detergents typically contain chelators to bind divalent cations from the washing water and lower the water hardness. Therefore, we sought to generate *Psp*Xan9 variants with high stability and activity in the absence of calcium ions. To do this, several variants were generated based on selecting positions shown as either having high mobility in the HDX-MS data, or being predicted to lie adjacent to those regions on the basis of modelling. At each position, saturation mutagenesis was performed. The activity and stability of the variants were evaluated by measuring residual activity and half-life improvement factors (HIF) (Table 2).

Table 2. Variants with improved stability after incubation in liquid detergent

Variant/ Mutation	Residual activity (%)	HIF
N966C	39 (3)	1.24 (0.06)
K1031I	39 (1)	1.23 (0.04)
S636M	37 (3)	1.17 (0.15)
K627Q	37 (2)	1.19 (0.07)
A559H	45 (5)	1.43 (0.08)
Wild type	32 (2.6)	1.00 (0.04)

Numbers in parentheses indicate standard deviations.

Variants were incubated in a liquid model detergent (Table S5) (70% detergent concentration) at either 4 or 30 °C for 22 h. After incubation, the enzyme activity on xanthan-lyase treated xanthan gum was determined, and residual activities were calculated as $Act_{30°C}/Act_{4°C}$ x 100%. Based on the residual activities after incubation at 30 °C, half-life ($T_{1/2}$) and half-life improvement factors ($T_{1/2variant}/T_{1/2native\ enz}$) were calculated (Table 2).

Comparative HDX-MS analysis of Ca^{2+}-bound and Ca^{2+}-depleted *Psp*Xan9 showed that regions most impacted by Ca^{2+} depletion were the β3 domain and the CBM84 domain as they encompass the peptides displaying the higher deuterium uptake differences upon Ca^{2+} removal (Table S4). Other, less pronounced effects were observed in the GH9 catalytic domain (for example regions 95-105, 227-251 and 291-296) (Table S4). Finally, several inter domain loops showed increased deuterium uptake upon Ca^{2+} depletion: segments 551-569 (connecting the GH9 and β1 domains), 639-660 (connecting the β1and β2 domains) and 809-822 (connecting the β2 and β3 domains) (Table S4).

Saturation mutagenesis (not shown) at two positions of the CBM84 domain yielded variants N966C and K1031I which showed high half-life improvement factors (HIF 1.24 and HIF 1.23) highlighting the benefit of targeting mobile regions in the comparative HDX-MS K1031I seems to be adjacent to all dynamic segments while N966C is adjacent to segments 928-959 and 980-989 that are closest to the mutation site in sequence and within the structure.

Similarly, S636M and K627Q are both located in the β1 domain, which also has a conformation that is closely tied to a coordinating Ca^{2+} ion. On top of this, both mutations neighbor region 639-660, which showed increased deuterium uptake upon Ca^{2+} removal (Table S4). The activity stabilizing effect of S636M and K627Q (HIF 1.17 and HIF 1.19) is therefore presumably linked to the stabilization of this Ca^{2+}-dependent region in the β1 domain.

The A559H mutation displayed the highest stabilizing effect (HIF 1.43). A559H is also located in the β1 domain; however, unlike S636M and K627Q, the A559H mutation is in a loop connecting the β1 and the GH9 domains. Thus, this mutation is much further from the 639-660 region and the Ca^{2+} ion than S636M and K627Q. The peptide segment encompassing A559H displays fast

deuterium uptake (residues 554-566, up to 50% at 15 s and 90% at 1 h) indicating considerable dynamics and flexibility of this loop region. By successfully increasing the stability of this inter-domain loop, A559H may thereby have enhanced the overall stability of the enzyme. Furthermore, residues 554-566 display a slight increase in deuterium uptake upon Ca^{2+} removal at the 10 min time point (Table S4) suggesting that this loop region is linked to the Ca^{2+} binding site despite the mutation site being further from it. In the structure, the loop is tethered close to the region coordinating the Ca^{2+} ion and thus by stabilizing the loop the mutation appears to have indirectly stabilized the Ca^{2+} binding site.

CONCLUSIONS

The increasing application of diverse polysaccharides in industrial and societal processes demands improved knowledge of the biological catalysts that synthesize, modify and degrade these polysaccharides. The polysaccharide xanthan is a prime example. Its gel-like properties mean that it finds astonishingly diverse application, not only in food production but also in pharmaceutical formulation and petroleum extraction. There is therefore a need to find catalysts capable of degrading this unusual polysaccharide. Here we have reported the identification of and defining 3-D structure for a new class of xanthan degrading enzyme – hydrolytic *endo*-xanthanases. We have shown that the enzyme has an unusual, multi-domain, 3-D structure with an open active center cleft that is able to bind and degrade polymeric xanthan in a processive manner. Industrial application xanthanases, indeed most glycoside hydrolases, often requires unusual conditions, placing additional stability demands on the catalyst. Here we have demonstrated the power of the H/D exchange method to identify regions of high mobility in both the presence and absence of Ca^{2+}, as well as to inform rational protein engineering approaches to enzyme stability which led to catalysts with improved half-lives in relevant conditions. The *Paenibacillus* GH9 *endo*-

processive xanthanase thus provides not only a first insight into nature's hydrolytic pathway for xanthan degradation but provides a blueprint for the rational redesign of enzymes, one of a number of tools that now allow the improvement of enzymes for societal benefit.

EXPERIMENTAL

Cloning, Expression and Purification

The *Psp*Xan9 gene was inserted into a *Bacillus* expression plasmid, essentially as described for a phospholipase [36] with an affinity tag sequence to easy the purification process. Briefly, the DNA encoding the mature polypeptide predicted by Signal P [37] was cloned in frame to the *Bacillus clausii* secretion signal, BcSP, replacing the native secretion signal sequence followed by a polyhistidine tag (HHHHHHPR). This resulted in a recombinant mature polypeptide with the His-tag (HHHHHHPR) in front of the N-terminus of the mature wild type sequence. A recombinant *B. subtilis* clone containing the integrated expression construct was selected and cultivated on a rotary shaking table in ten 500 mL baffled Erlenmeyer flasks each containing 100 mL LB media supplemented with 34 $mg \cdot L^{-1}$ chloramphenicol. The clone was cultivated for 5 days at 30 °C. The enzyme-containing supernatants were separated from the cells by centrifuging the culture broth for 30 min at 15.000 × *g* and the enzyme was purified as described below.

The decanted supernatant was mixed with ammonium sulfate and Tris-HCl, pH 7.5 to obtain a final ammonium sulfate concentration of 800 mM in 20 mM Tris-HCl, pH 7.5. The sample was incubated for 30 min at room temperature with continuous stirring. Precipitate and bacterial cells

were removed by passing the sample through a 0.2 μm Nalgene filtration system. Column chromatography was done by using an AKTA Explorer FPLC (GE Healthcare). The filtered sample was loaded on a 50 mL Phenyl Sepharose High Performance column (GE Healthcare, Uppsala, Sweden) equilibrated in 20 mM Tris-HCl, pH 7.5, 800 mM ammonium sulfate. Proteins were eluted by step elution with 20 mM Tris-HCl, pH 7.5. Eluted fractions were analyzed using SDS-PAGE and fractions eluting at 280 mM ammonium sulfate were pooled. The pool was applied on a 20 mL HisPrep fast flow column (GE Healthcare) equilibrated with 500 mM NaCl, 20 mM Tris-HCl, pH 8.5. Proteins were eluted by a linear gradient using 500 mM NaCl, 500 mM imidazole, 20 mM Tris-HCl, pH 7.5. Eluted fractions were analyzed by SDS-PAGE. Fractions with increased purity were pooled and buffer exchanged to 20 mM Tris-HCl, pH 8.5 by using a 340 mL G25 superfine desalting column. The desalted sample was applied on a 20 mM Source 15Q column equilibrated in 20 mM Tris-HCl, pH 8.5. Elution was done by a linear gradient from 0.0 to 200 mM NaCl in the same buffer over 4 column volumes. The purity of the eluted fractions was evaluated using SDS-PAGE and fractions judged as > 95% pure were pooled and buffer exchanged to 20 mM Tris-HCl, pH 8.5. The intact protein mass of these samples was determined to be 115972 Da using a nanoACQUITY UPLC/Xevo Q-TOF MS system, essentially according to methods previously described [38] (Figure S16). Protein concentration was calculated from A_{280} values using the theoretical extinction coefficient of 199860 $M^{-1}cm^{-1}$ based on the deduced mature amino acid sequence.

Site-directed variants of mature *Psp*Xan9 were engineered by the megaprimer mutagenesis method using specifically designed mutagenic oligonucleotides introducing desired mutations in the resulting sequence. Consequently, mutagenic oligonucleotides were designed and synthesized

corresponding to the DNA sequence flanking the desired site(s) of mutation, separated by the DNA base pairs defining the substitutions. The final expression cassette composed the *Psp*Xan9 gene as described above. Successful introduction of the desired substitutions was confirmed by DNA sequencing of the *Psp*Xan9 variant gene. An aliquot of the PCR product was subsequently transformed into *Bacillus subtilis*. Transformants were selected on LB agar plates supplemented with 10 mM K_2PO_4, 0.4% extra glucose and 6 $\mu g \cdot mL^{-1}$ of chloramphenicol. The resulting recombinant *Bacillus subtilis* clones containing the integrated expression construct were grown in liquid TB-glycerol medium containing a standard trace metal mix[39] for 4 days at 30°C before harvested and purified as for the mature *Psp*Xan9 described above.

Carbohydrate Sources

Xanthan gum (item no. XA105), referred to herein as "native, polypentameric xanthan" (Figure 1), was purchased from Spectrum Chemical, New Brunswick, NJ, USA. Barley mixed-linkage glucan (bMLG), tamarind seed xyloglucan (tXyG), beechwood xylan (bGX) and wheat-flour arabinoxylan (wAX) were purchased from Megazyme (Bray, Ireland). Carboxymethylcellulose (CMC) was purchased from Acros Organics (Morris Plains, NJ, USA). Hydroxyethylcellulose (HEC) was purchased from Amresco (Solon, OH, USA). "Lyase-treated xanthan" (Figure 1) was prepared by xanthan lyase treatment of native, polypentameric xanthan essentially according to a method described previously[9]. Briefly, xanthan gum was dissolved in 50 mM HEPES-NaOH buffer, pH 7.0, to a concentration of 2.5 $g \cdot L^{-1}$ and treated with 0.5 $U \cdot mL^{-1}$ of *Bacillus* sp. xanthan lyase (EC 4.2.2.12, CAZy Family PL8, Megazyme cat. no. E-XANLB). The formation of Δ4,5-ene-glucuronyl residues was monitored using a Cary 60 UV-visible spectrometer with a 1-cm path length quartz cuvette at an absorbance of 235 nm [6]. Once the A_{235} value reached a plateau, an additional 0.5 U ▪ $\cdot mL^{-1}$ of xanthan lyase was added and the reaction was monitored to ensure

completeness. Lyase-treated xanthan was purified by precipitation essentially as previously described[6, 9], except ice cold 2-propanol was used instead of ethanol, and the mixture was centrifuged at 4500 × *g* for 20 min to aid in supernatant removal. The precipitated lyase-treated xanthan was placed in a vacuum desiccator for 72 h to remove residual 2-propanol prior to dissolution in ultrapure H_2O for enzyme assays.

Enzyme Kinetic Analysis

Enzyme kinetics on soluble polysaccharides were determined by quantifying the generation of new reducing chains ends using a copper/2,2'-bicinchoninic acid (BCA) assay in an optimized, low volume format[40]. D-Glucose standard curves were measured between 0 and 125 μmol in 50 mM HEPES-NaOH, pH 7, with or without 2 mM $CaCl_2$, as appropriate. To reduce the nonspecific absorption of enzyme on vessel surfaces, suitably diluted *Psp*Xan9 was premixed with 0.1 $mg \cdot mL^{-1}$ bovine serum albumin (BSA) in 5 mM HEPES-NaOH buffer, pH 7, unless otherwise specified; this solution was ultimately diluted 10-fold into the assay solution. In general, assays were initiated by the addition of enzyme after preheating substrate in buffer to the desired temperature for at least 15 min. Reactions were terminated by the addition of ice cold BCA reagent at a 1:1 v/v ratio and concentrations of the Cu^+-BCA complex were determined from A_{562} measurements.

All reactions to optimize activity were conducted using 0.5 $mg \cdot mL^{-1}$ of lyase-treated xanthan based on preliminary results[24]. The effect of calcium ions on activity was determined by incubating 1.59 nM *Psp*Xan9 with lyase-treated xanthan at 37 °C in 50 mM HEPES-NaOH buffer, pH 7.0, containing 0-10 mM $CaCl_2$. The optimal temperature for activity was determined by incubating a

final enzyme concentration of 0.8 nM with lyase-treated xanthan in the 50 mM HEPES-NaOH buffer, pH 7.0, between 30 °C and 78 °C. The pH rate profile was characterized by incubating 0.8 nM of enzyme with lyase-treated xanthan at 55 °C in selected buffers (50 mM) between pH 3.6-10.6. The buffer and pH range used were as follows: sodium acetate, pH 3.6-5.5; MES, pH 5.38-7.0; HEPES-NaOH, pH 7.0-8.5; CHES, pH 8.5-10.6.

The effect of Ca^{2+} ions on thermostability of *Psp*Xan9 maintained at temperatures between 45 °C and 69°C (Bio-Rad Thermal Cycler S1000) was determined by incubating 16 nM of the enzyme in the presence or absence of 20 mM CaCl2 and measuring remaining hydrolytic activity toward 0.5 $mg \cdot mL^{-1}$ lyase-treated xanthan over time. The conditions of the BCA assay were adjusted to ensure that all assay solutions contained a final concentration of 2 mM $CaCl_2$ following the addition of enzyme to initiate the reaction (1:10 dilution of *Psp*Xan9 in assay).

Enzyme specific activity was determined for selected substrates by incubating 2 $mg \cdot mL^{-1}$ native polypentameric xanthan, lyase-treated xanthan, bMLG, tXyG, bGX, wAX, bMLG, CMC, or HEC with *Psp*Xan9 at 55 °C in 50 mM HEPES-NaOH buffer, pH 7.0. The *Psp*Xan9 concentration in the assay was 0.4 nM for lyase-treated xanthan, 191 nM for polypentameric xanthan and CMC, and 383 nM for all other polysaccharides. One unit of activity (U) is defined as the amount of enzyme required to release 1 μmol of glucose-equivalent reducing ends per minute. Controls containing heat-inactivated (incubation at 90 °C for 20 min) *Psp*Xan9 were used to account for high background absorbance resulting from high protein concentration in some samples. Apparent Michaelis-Menten kinetic parameters were determined for lyase-treated xanthan by treating reaction mixtures at 55 °C containing substrate concentrations between 0.01-2 $mg \cdot mL^{-1}$ lyase-treated xanthan with 0.4 nM of enzyme. Data were fit with the Michaelis-Menten equation using OriginPro software (OriginLab).

Enzyme Product Analysis

Partial hydrolysis products were obtained by incubation at 55 °C of 16 nM *Psp*Xan9 and 2 mg·mL^{-1} lyase-treated xanthan in 50 mM HEPES-NaOH, pH 7, containing 2 mM $CaCl_2$. Following heat inactivation, samples were analyzed by HPSEC-UV on an ICS-5000 DC HPLC system operated using Chromeleon software version 7 (ThermoFisher). Samples were eluted through a UltrahydrogelTM 6 x 40 mm Guard Column in series with a Ultrahydrogel^{TM} Linear 7.8 x 300 mm column using 0.5 M NaCl at 0.6 mL·min^{-1} for 45 min. Elution was monitored by absorbance at 235 nm.

Mass spectrometric analysis of the partial hydrolysis products following 2 h of reaction incubation was performed using a nanoACQUITY UPLC coupled to a Xevo G2-S QTof (Waters Co., Milford, MA, USA). Oligosaccharide separation was achieved using a Hypercarb Kappa 3 μm porous graphitized carbon column (150 x 0.32 mm). Eluent A comprised 95% 25 mM ammonium formate, pH 5, and 5% acetonitrile; eluent B comprised 5% 0.5 M ammonium formate, pH 5, and 95% acetonitrile. Samples were eluted at a flow rate of 8 μL·min^{-1} with the following gradient: 0-5 min: 95% eluent A and 5% eluent B; 5-25 min: linear gradient to 70% eluent A and 30% eluent B; 25-25.1 min: linear gradient to 95 % eluent A and 5% eluent B; 25.1-45 min: 95% eluent A and 5% eluent B. Mass spectra were collected in negative-ion mode, with a 2 s integration time. Collision induced dissociation of the target masses of 661 *m/z* and 703 *m/z* were performed using a collision energy of 15 eV. To determine the relative position of the branch in *Psp*Xan9 xanthanase products, the hydrolysis reaction was allowed to go to completion and the limit-digest products were diluted to 1 mg·mL^{-1} with 50 mM sodium carbonate buffer, giving a final pH of 10. $NaBH_4$ (S678-25, Fisher Scientific) was added to a final concentration of 1 M and incubated at room temperature for 12 h before the quenching by the addition of 1 M acetic acid to give a slightly acidic pH (5-6). The

reduced oligosaccharides were analyzed by mass spectrometry using the same method as described above, only the final isocratic gradient was reduced to 25.1-30 min and collision energy was set to 25 eV with a target mass of 663 *m/z*.

Unsaturated xanthan tetrasaccharides were prepared for NMR by performing a limit digest on 12.5 $mg \cdot mL^{-1}$ lyase-treated xanthan using 38 nM of *Psp*Xan9 with 2 mM $CaCl_2$ in 5 mM HEPES-NaOH buffer pH 7.0. Full product conversion was confirmed using HPSEC-UV before the pH was then raised to 10 using 28-30% NH_4OH (1336-21-6, Fisher Scientific) to deacetylate the sample. The deacetylated sample was lyophilized and resuspended in H_2O before being desalted into ultra-pure H_2O using a 100 x 2.6 cm Bio-Gel P-2 column at a flow rate of 0.5 $mL \cdot min^{-1}$. Fractions absorbing at 235 nm were pooled and lyophilized. The sample was resuspended in 500 µL of 99.9% D_2O and lyophilized, twice. Finally, 3.5 mg of the unsaturated xanthan tetrasaccharide was dissolved in 500 µL of D_2O. NMR experiments were performed using a Bruker Avance 600 equipped with a z-gradient TCI cryoprobe, with a ^{1}H resonance at 600.15 MHz and a ^{13}C resonance of 150.92 MHz. A 1D-^{1}H NMR spectrum and selective ^{1}H 1D-TOCSY NMR spectra with irradiation at 4.29, 4.44, 4.64, 5.20 and 5.36 ppm followed by 0.12 ms of mixing time were collected. 2D-^{1}H TOCSY, COSY and ^{1}H,^{13}C HSQC spectra were collected, as well as ^{1}H,^{13}C HMBC experiments which were optimized for coupling at 5 and 10 Hz. All ^{1}H experiments were referenced to the HOD peak (δ 4.70 ppm) and all ^{13}C experiments were referenced to external methanol in D_2O (δ 49.00 ppm).

Crystallization and Data Collection

Initial crystallization screening was carried out at room temperature using sitting-drop vapor diffusion set up using a *Mosquito Crystal* liquid handling robot (TTP LabTech, UK) with 150 nL protein solution plus 150 nL reservoir solution in 96-well format plates (MRC 2-well crystallization microplate, Swissci, Switzerland) equilibrated against 54 μL reservoir solution, with a number of commercial screens. Initial crystals were obtained in PACT condition E12: 20% PEG3350, 0.2 M sodium malonate. Native data were collected at Diamond I04-1 to 2.04 Å resolution and processed by *xia2*[41] space group $P3_221$, with one molecule in the asymmetric unit. Crystallization conditions were manually optimized to produce crystals for heavy atom soaks, with final conditions 20-22% PEG3350 and 0.1 M Bis-Tris propane pH 6.5. The crystals were transferred to conditions similar to those in which they were grown, but with 2-5% increased PEG3350 concentration, and 2-5 mM heavy atom compounds. Several potential derivatives were screened; the one that proved successful was $K_2Pt(SCN)_4$. Derivative data were collected at Diamond, beamline I03, to 2.0 Å resolution, and were in the same space group as the native with closely similar cell dimensions.

Structure Solution and Refinement

All computations were carried out using programs from the *CCP4* suite[42], unless otherwise stated. The structure was solved by single wavelength anomalous diffraction method (SAD) using the Crank pipeline[43], with AFRO/CRUNCH2 [44] for substructure detection, BP3 [45-46]for substructure refinement, SOLOMON [47] for hand determination and density modification and BUCCANEER [48] for model building. The model for the derivative was further refined with REFMAC5 [49] iterated with manual model building with COOT[50]. The native structure was refined using the derivative structure as a starting model. TLS was used in the refinement for both structures[51], with the domain

allocation shown in Figure 3a. Both structures were validated using PROCHECK [52] and MOLPROBITY[53], and the processing and refinement statistics are given in Table S2.

H/D Exchange Mass Spectrometry

Continuous amide H/D exchange of *Psp*Xan9 at a concentration of 1 μM and 22 °C was initiated by addition of 99.9% deuterated 20 mM Tris, 1 mM $CaCl_2$, pH 8 in the absence or presence of 10 mM EDTA to a final deuterium concentration of 95%. All H/D exchange reactions were performed in triplicate. At five time points ranging from 15 s to 1 h, aliquot samples of the exchange reaction were quenched by addition of 1:1 (v/v) ice-cold 6 M guanidinium hydrochloride, 300 mM phosphate, pH 2.05 for a final pH of 2.6. The quenched samples were frozen immediately and stored at −80 °C until LC-MS analysis. Non-deuterated samples were prepared following the same procedure but using protiated buffers. Equilibrium deuterated samples (95% D_2O) were prepared by over-night incubation in 99.9% deuterated 6 M guanidinium hydrochloride and quenched in 300 mM phosphate, pH 2.3 for a final pH of 2.6. The quenched samples were loaded into a cooled HDX-UPLC system (Waters, Milford, USA) for online pepsin digestion using an immobilized pepsin column (Pierce, Rockford, USA). The peptides were desalted using a trap column (Waters VanGuard C18, 1.7 μM, 2.1 x 5 mm) at a flow of 200μl/min 0.23% formic acid for 3 min and peptides were separated by reverse phase chromatography (Waters Acquity BEH C18, 1.7 μm, 1 x 100 mm) using a two-step gradient from 8-18% in 2 min and 18-40% in 10 min 0.23% formic acid in acetonitrile at a flow of 40 $\mu l \cdot min^{-1}$. Positive electrospray ionization mass spectrometry with ion mobility was performed on the peptides using a Synapt G2 mass spectrometer (Waters, Milford, USA).

The peptic peptides of *Psp*Xan9 were identified by tandem mass spectrometry of non-deuterated samples using a combination of data independent (DIA/MSe) and data dependent acquisition schemes (DDA) and data-analysis in Protein Lynx Global Server v. 2.5. Deuterium uptake of individual peptides was determined using DynamX v. 3.0 (Waters, Milford, USA) or in HXexpress[54]. Statistical analysis (F-tests and student T-tests) were employed to determine statistically significant changes in H/D exchange between the analyzed protein states.

Detergent Stability

To assess the detergent stability of *Psp*Xan9 and variants, 0.1 $mg \cdot mL^{-1}$ purified protein was incubated with liquid detergent (see Table S5, 70% detergent concentration) at either 4 °C or 30 °C for 22 h. After incubation, samples from 4 respective 30 °C incubation were transferred into 96-well plates and further diluted 50 times with dilution buffer (50 mM MOPS, 5 mM $CaCl_2$, pH 7.5). Reaction mixtures were prepared in 96-well PCR plates by mixing 50 µL of 50 times diluted protein samples with 50 µL of freshly prepared lyase-treated polytetrameric xanthan solution (0.4% in MilliQ water) and incubated at 48 °C for 1 h. After incubation, 75 µL of PAHBAH reagent (15 $mg \cdot mL^{-1}$ 4-hydroxybenzoic acid hydrazide (PAHBAH), 50 $mg \cdot min^{-1}$ potassium sodium tartrate tetrahydrate, 20 $mg \cdot mL^{-1}$ NaOH) was added to each reaction mixture in the same PCR plate and incubated further in a programmable thermal cycler for 10 min at 95 °C followed by cooling at 10 °C. 40 µL of each reaction mixture was transferred to a 384-well microtiter plate and the absorbance was measured at 405 nm using a spectrophotometer. The residual enzyme activity was calculated as $Act_{30°C}/Act_{4°C}$ x 100%. Based on the residual activities after incubation at 30 °C, half-lives ($T_{1/2}$) and half-life improvement factors ($T_{1/2variant}/T_{1/2native\ enz}$) were calculated (Table 2).

ASSOCIATED CONTENT

The following files are available free of charge.

Details of enzyme characterization and product analysis (PDF)

AUTHOR INFORMATION

Corresponding Author

* Keith S. Wilson: keith.wilson@york.ac.uk

* Harry Brumer: brumer@msl.ubc.ca

* Kasper Rand: kasper.rand@sund.ku.dk

ORCID

Gideon Davies: 0000-0002-7343-776X

Keith Wilson: 0000-0002-3581-2194

Kasper Rand: 0000-0002-6337-5489

Author Contributions

[=]OVM, PFJ & SPM contributed equally. SPM performed enzymology, MS, and NMR experiments, analyzed the resulting data, and co-wrote the article. OVM and EB carried out the crystal screening and structure analysis. NM assisted with MS data acquisition and analysis. HB supervised research at UBC, analyzed data, and co-wrote the article. DRS, LA, SMV, VPR, THS and LG performed the experiments (cloning, expression, variant generation, purification, detergent stability and CBM binding); RNM, AS and JEN planned the experiments and co-wrote the article. PFJ planned and performed HDX-MS experiments, analyzed data and co-wrote the article. GK analyzed HDX-MS data and co-wrote the article. KDR planned HDX-MS experiments, analyzed data and supervised research at UCPH. KSW and GJD supervised the structural biology and co-wrote the article.

Funding Sources

Work at University of Copenhagen was supported by the Danish Council for Independent Research (Sapere Aude grant no. 4184-00537A). Work at the University of British Columbia was supported by the Natural Sciences and Engineering Research Council of Canada (Discovery Grant), the Canada Foundation for Innovation, and the British Columbia Knowledge Development Fund. Gideon Davies is a Royal Society Ken Murray Research Professor

Conflict of Interest Declaration

Novozymes A/S are a commercial enzyme supplier

ABBREVIATIONS

GH, glycoside hydrolase; PL, polysaccharide lyase; bMLG, barley mixed-linkage glucan; tXyG, tamarind xyloglucan; bGX, beechwood glucuronoxylan; wAX, wheat flour arabinoxylan; CMC, carboxymethylcellulose; HDX-MS, hydrogen/deuterium exchange coupled with mass spectrometry; HEC, hydroxyethylcellulose; BCA, 2,2' bicinchoninic acid; BSA, Bovine serum albumin; HPSEC UV, high performance size-exclusion chromatography with UV detection; LC-ESI-MS, liquid chromatography coupled with electrospray ionization mass spectrometry; LC-MS/MS, liquid chromatography coupled with tandem mass spectrometry; TOCSY, total correlation spectroscopy; COSY, correlation spectroscopy; Glc(r.), reducing end glucose; Glc(n.r.), nonreducing end glucose; Man, mannose; Δ4,5-*ene*-GlcA / Δ4,5-GlcA, Δ4,5-*ene*-glucuronic acid; HSQC, heteronuclear single quantum correlation spectroscopy; HMBC heteronuclear multiple-bond correlation spectroscopy; SAD, single wavelength anomalous diffraction; PDB, Protein Data Bank; CBM, carbohydrate binding models; Ig, immunoglobulin; r.m.s.d., root mean square deviation; UNK, unknown

ACKNOWLEDGMENT

We thank Diamond Light Source for access to beamlines I04-1 and I03 (proposal number mx-7864) that contributed to the results presented here.. We thank Johan Turkenburg and Sam Hart for support with the X-ray data collection. We thank Dr. Lorena G. Palmen, Dr. Shikha Gupta, Dr. Partha P. Chakrabarti, Dr. Sohel Dalal and Marie T. Kruse (Novozymes) for technical assistance and discussions. Waters Corp. is gratefully acknowledged for the provision of the LC-MS system used in this study. We thank Dr. Gregory Arnal (Brumer group) for technical discussions regarding enzyme assays and Dr. Wei Qiang (Ben) Hui (Brumer group) and Dr. Maria Ezhova (UBC Chemistry) for NMR assistance.

REFERENCES

1. Katzen, F.; Ferreiro, D. U.; Oddo, C. G.; Ielmini, M. V.; Becker, A.; Puhler, A.; Ielpi, L., *Xanthomonas campestris* pv. *campestris* gum mutants: Effects on xanthan biosynthesis and plant virulence *J. Bacteriol*. **1998,** *180*, 1607-1617.

2. Schmid, J.; Sieber, V.; Rehm, B., Bacterial exopolysaccharides: biosynthesis pathways and engineering strategies *Frontiers Microbiol* **2015,** *6*, 24.

3. Ates, O., Systems Biology of Microbial Exopolysaccharides Production *Front Bioeng Biotechnol* **2015,** *3*, 200.

4. Lopes, B. M.; Lessa, V. L.; Silva, B. M.; Carvalho Filho, M. A. S.; Schnitzler, E.; Lacerda, L. G., Xanthan gum: properties, production conditions, quality and economic perspective. *J Food Nutrit Res* **2015,** *54*, 185-194.

5. Jansson, P.-E.; Kenne, L.; Lindberg, B., Structure of the extracellular polysaccharide from *Xanthomonas campestris*. *Carbohydr. Res*. **1975,** *45*, 275-282.

6. Ruijssenaars, H. J., de Bont, J.A.M., and Hartmans, S., A pyruvated mannose-specific xanthan lyase involved in xanthan degradation by *Paenibacillus alginolyticus* XL-1. 65 *Appl Environ Microbiol* **1999,** *65*, 2446-2452.

7. Garcia-Ochoa, F.; Santos, V. E.; Casas, J. A.; Gomez, E., Xanthan gum: production, recovery, and properties *Biotechnol. Adv*. **2000,** *18*, 549-579.

8. Sutherland, I. W., *Xanthomonas* polysaccharides — Improved methods for their comparison *Carbohydr. Polym*. **1981,** *1*, 107-115.

9. Nankai, H.; Hashimoto, W.; Miki, H.; Kawai, S.; Murata, K., Microbial System for polysaccharide depolymerisation: enzymatic route for xanthan depolymerisation by *Bacillus* sp. strain GL1. *Appl Environ Microbiol* **1999,** *65*, 2520-2526.

10. Sutherland, I. W., Xanthan Lyases - Novel Enzymes Found in Various Bacterial Species *J. Gen. Microbiol*. **1987,** *133*, 3129-3134.

11. Cadmus, M. C.; Slodki, M. E., Enzymic Breakage of Xanthan Gum Solution Viscosity in the Presence of Salts. *Develop Indust Microbiol* **1985,** *26*, 281-289.

12. Cadmus, M. C.; Slodki, M. E.; Nicholson, J. J., High-temperature, salt-tolerant xanthanase. *J. Ind. Microbiol*. **1989,** *4*, 127-133.

13. Ahlgren, J. A., Purification and properties of a xanthan depolymerase from a heat-stable salt-tolerant bacterial consortium. *J. Ind. Microbiol.* **1993,** *12*, 87-92.

14. Hou, C., T.; Barnabe, N.; Greaney, K., Purification and properties of a novel xanthan depolymerase from a salt-tolerant bacterial culture, HD1 *Appl. Environ. Microbiol.* **1986,** *52*, 37-44.

15. Yang, F., Li, L., Si, Y., Yang, M., Guo, X., Hou, Y., Chen, X., Li, X., Complete genome sequence of a xanthan-degrading *Microbacterium* sp. strain XT11 with the potential for xantho-oligosaccharides production *J. Biotechnol.* **2016,** *222*, 19-20.

16. Ahlgren, J. A., Purification and Characterization of a Pyruvated-Mannose-Specific Xanthan Lyase from Heat-Stable, Salt-Tolerant Bacteria *Appl. Environ. Microbiol.* **1991,** *57*, 2523-2528.

17. Hashimoto, W.; Miki, H.; Tsuchiya, N.; Nankai, H.; Murata, K., Xanthan lyase of Bacillus sp. strain GL1 liberates pyruvylated mannose from xanthan side chains *Appl. Environ. Microbiol.* **1998,** *64*, 3765-3768.

18. Lombard, V.; Bernard, T.; Rancurel, C.; Brumer, H.; Coutinho, P. M.; Henrissat, B., A hierarchical classification of polysaccharide lyases for glycogenomics *Biochem. J* **2010,** *432*, 437-444.

19. Maruyama, Y.; Mikami, B.; Hashimoto, W.; Murata, K., A structural factor responsible for substrate recognition by *Bacillus* sp. GL1 xanthan lyase that acts specifically on pyruvated side chains of Xanthan *Biochemistry* **2007,** *46*, 781-791.

20. Hashimoto, W.; Nankai, H.; Mikami, B.; Murata, K., Crystal structure of *Bacillus* sp. GL1 xanthan lyase, which acts on the side chains of xanthan *J. Biol. Chem.* **2003,** *278*, 7663-7673.

21. Maruyama, Y.; Hashimoto, W.; Mikami, B.; Murata, K., Crystal structure of *Bacillus* sp. GL1 xanthan lyase complexed with a substrate: Insights into the enzyme reaction mechanism *J. Mol. Biol.* **2005,** *350*, 974-986.

22. Li, B.; Guo, J. Q.; Chen, W. F.; Chen, X. Y.; Chen, L. G.; Liu, Z. W.; Li, X. Z., Endoxanthanase, a Novel beta-d-Glucanase Hydrolyzing Backbone Linkage of Intact Xanthan from Newly Isolated *Microbacterium* sp. XT11 *Appl. Biochem. Biotechnol.* **2009,** *159*, 24-32.

23. Wilson, D. B.; Urbanowicz, B., Glycoside Hydrolase Family 9 *in CAZypedia*, URL: http://www.cazypedia.org/index.php/Glycoside_Hydrolase_Family_9 (10 October 2016).

24. Segura, D. R., Halin, P. F., Viksoe-Nielsen, A., Anderson, L., Borchert, M. S., Murphy, L., Boisen, A., Palmén, L. G., Jensen, K., Sjoeholm, C., Hoff, T., Blom, C. Polypeptides having xanthan degrading activity and polynucleotides encoding same. WO/2013/167581, 2013.

25. Madsen, K. R.; Segura, D. R.; Boisen, A.; Murphy, L.; Anderson, L.; Palmen, L. G. Polypeptides with xanthan lyase activity having anti-redeposition effect and polynucleotides encoding same. WO/2015/001017, 2015.

26. Eklof, J. M.; Ruda, M. C.; Brumer, H., Distinguishing xyloglucanase activity in endo-beta(1->4)glucanases *Methods Enzymol*. **2012,** *510*, 97-120.

27. Mikkonen, K. S.; Tenkanen, M., Sustainable food-packaging materials based on future biorefinery products: Xylans and mannans *Trends Food Sci. Technol*. **2012,** *28*, 90-102.

28. Agrawal, P. K., NMR Spectroscopy in the structural elucidation of oligosaccharides and glycosides *Phytochemistry* **1992,** *31*, 3307-3330.

29. Bubb, W. A., NMR spectroscopy in the study of carbohydrates: Characterizing the structural complexity *Concepts Magn Reson Part A* **2003,** *19A*, 1-19.

30. Cheetham, N. W. H.; Mashimba, E. N. M., Proton and carbon-13 NMR studies on xanthan derivatives *Carbohydr. Polym*. **1992,** *17*, 127-136.

31. Kool, M. M.; Gruppen, H.; Sworn, G.; Schols, H. A., Comparison of xanthans by the relative abundance of its six constituent repeating units *Carbohydr. Polym*. **2013,** *98*, 914-921.

32. Krissinel, E.; Henrick, K., Secondary-structure matching (SSM), a new tool for fast protein structure alignment in three dimensions *Acta Crystallogr. Sect. D. Biol. Crystallogr*. **2004,** *60*, 2256-2268.

33. McNicholas, S.; Potterton, E.; Wilson, K. S.; Noble, M. E., Presenting your structures: the CCP4mg molecular-graphics software *Acta Crystallogr. Sect. D. Biol. Crystallogr*. **2011,** *67*, 386-94.

34. Davies, G.; Henrissat, B., Structures and Mechanisms of Glycosyl Hydrolases *Structure* **1995,** *3*, 853-859.

35. Mandelman, D.; Belaich, A.; Belaich, J. P.; Aghajari, N.; Driguez, H.; Haser, R., X-ray crystal structure of the multidomain endoglucanase Cel9G from Clostridium cellulolyticum complexed with natural and synthetic cello-oligosaccharides *J. Bacteriol*. **2003,** *185*, 4127-4135.

36. Moroz, O. V.; Blagova, E.; Lebedev, A. A.; Norgaard, A.; Segura, D. R.; Blicher, T. H.; Brask, J.; Wilson, K. S., The structure of a calcium-dependent phosphoinositide-specific

phospholipase C from Pseudomonas sp. 62186, the first from a Gram-negative bacterium *Acta Crystallogr. Sect. D. Biol. Crystallogr.* **2017,** *73*, 32-44.

37. Bendtsen, J. D.; Nielsen, H.; von Heijne, G.; Brunak, S., Improved prediction of signal peptides: SignalP 3.0 *J. Mol. Biol.* **2004,** *340*, 783-95.

38. Konermann, L.; Pan, J. X.; Liu, Y. H., Hydrogen exchange mass spectrometry for studying protein structure and dynamics *Chem. Soc. Rev.* **2011,** *40*, 1224-1234.

39. Studier, F. W., Protein production by auto-induction in high density shaking cultures *Protein Expr Purif* **2005,** *41*, 207-34.

40. Arnal, G.; Attia, M. A.; Asohan, J.; Brumer, H., A low-volume, parallel copper-bicinchoninic acid (BCA) assay for glycoside hydrolases *Methods Mol Biol* **2017,** *1588*, 3-14.

41. Winter, G., xia2: an expert system for macromolecular crystallography data reduction *J. Appl. Crystallogr.* **2010,** *43*, 186-190.

42. Winn, M. D.; Ballard, C. C.; Cowtan, K. D.; Dodson, E. J.; Emsley, P.; Evans, P. R.; Keegan, R. M.; Krissinel, E. B.; Leslie, A. G.; McCoy, A.; McNicholas, S. J.; Murshudov, G. N.; Pannu, N. S.; Potterton, E. A.; Powell, H. R.; Read, R. J.; Vagin, A.; Wilson, K. S., Overview of the CCP4 suite and current developments *Acta Crystallogr. Sect. D. Biol. Crystallogr* **2011,** *67*, 235-42.

43. Ness, S. R.; de Graaff, R. A. G.; Abrahams, J. P.; Pannu, N. S., CRANK: New methods for automated macromolecular crystal structure solution *Structure* **2004,** *12*, 1753-1761.

44. de Graaff, R. A. G.; Hilge, M.; van der Plas, J. L.; Abrahams, J. P., Matrix methods for solving protein substructures of chlorine and sulfur from anomalous data *Acta Crystallogr. Sect. D. Biol. Crystallogr.* **2001,** *57*, 1857-1862.

45. Pannu, N. S.; McCoy, A. J.; Read, R. J., Application of the complex multivariate normal distribution to crystallographic methods with insights into multiple isomorphous replacement phasing *Acta Crystallogr. Sect. D. Biol. Crystallogr* **2003,** *59*, 1801-1808.

46. Pannu, N. S.; Read, R. J., The application of multivariate statistical techniques improves single-wavelength anomalous diffraction phasing *Acta Crystallogr. Sect. D. Biol. Crystallogr* **2004,** *60*, 22-27.

47. Abrahams, J. P.; Leslie, A. G. W., Methods used in the structure determination of bovine mitochondrial F-1 ATPase *Acta Crystallogr. Sect. D. Biol. Crystallogr.* **1996,** *52*, 30-42.

48. Cowtan, K., The Buccaneer software for automated model building. 1. Tracing protein chains *Acta Crystallogr. Sect. D. Biol. Crystallogr.* **2006,** *62*, 1002-1011.

49. Murshudov, G. N.; Skubak, P.; Lebedev, A. A.; Pannu, N. S.; Steiner, R. A.; Nicholls, R. A.; Winn, M. D.; Long, F.; Vagin, A. A., REFMAC5 for the refinement of macromolecular crystal structures *Acta Crystallogr. Sect. D. Biol. Crystallogr* **2011,** *67*, 355-367.

50. Emsley, P.; Lohkamp, B.; Scott, W. G.; Cowtan, K., Features and development of Coot *Acta Crystallogr. Sect. D. Biol. Crystallogr* **2010,** *66*, 486-501.

51. Winn, M. D.; Isupov, M. N.; Murshudov, G. N., Use of TLS parameters to model anisotropic displacements in macromolecular refinement *Acta Crystallogr. Sect. D. Biol. Crystallogr.* **2001,** *57*, 122-133.

52. Laskowski, R. A.; Macarthur, M. W.; Moss, D. S.; Thornton, J. M., Procheck - a Program to Check the Stereochemical Quality of Protein Structures *J. Appl. Crystallogr.* **1993,** *26*, 283-291.

53. Chen, V. B.; Arendall, W. B., 3rd; Headd, J. J.; Keedy, D. A.; Immormino, R. M.; Kapral, G. J.; Murray, L. W.; Richardson, J. S.; Richardson, D. C., MolProbity: all-atom structure validation for macromolecular crystallography *Acta Crystallogr D Biol Crystallogr* **2010,** *66*, 12-21.

54. Guttman, M.; Weis, D.; Engen, J.; Lee, K., Analysis of Overlapped and Noisy Hydrogen/Deuterium Exchange Mass Spectra *J. Am. Soc. Mass. Spectrom.* **2013,** *24*, 1906-1912.